1   **The Cryo-EM Structure of a Pannexin 1 Reveals Unique Motifs for Ion Selection and**

2   **Inhibition**

3

4   Kevin Michalski[1*], Johanna L. Syrjanen[2*], Erik Henze[1], Julia Kumpf[1], Hiro Furukawa[2], and

5   Toshimitsu Kawate[1]

6

7   [1]Department of Molecular Medicine, Cornell University, Ithaca, NY USA

8   [2]WM Keck Structural Biology Laboratory, Cold Spring Harbor Laboratory, Cold Spring Harbor,

9   NY, USA

10   [*]These authors contributed equally

11

12   To whom correspondence should be addressed:

13   Hiro Furukawa: furukawa@cshl.edu

14   Toshimitsu Kawate: toshi.kawate@cornell.edu

Abstract

Pannexins are large-pore forming channels responsible for ATP release under a variety of physiological and pathological conditions. Although predicted to share similar membrane topology with other large-pore forming proteins such as connexins, innexins, and LRRC8, pannexins have minimal sequence similarity to these protein families. Here, we present the cryo-EM structure of a frog pannexin 1 (Panx1) channel at 3.0 Å. We find that Panx1 protomers harbor four transmembrane helices similar in arrangement to other large-pore forming proteins but assemble as a heptameric channel with a unique constriction formed by Trp74 in the first extracellular loop. Mutating Trp74 or the nearby Arg75 disrupt ion selectivity whereas altering residues in the hydrophobic groove formed by the two extracellular loops abrogates channel inhibition by carbenoxolone. Our structural and functional study establishes the extracellular loops as important structural motifs for ion selectivity and channel inhibition in Panx1.

Introduction

Large-pore forming channels play important roles in cell to cell communication by responding to diverse stimuli and releasing signaling molecules like ATP and amino acids (Giaume et al., 2013; Ma et al., 2016; Okada et al., 2018; Osei-Owusu et al., 2018). Pannexins are a family of ubiquitously expressed large-pore forming channels which regulate nucleotide release during apoptosis (Chekeni et al., 2010), blood pressure (Billaud et al., 2011; Billaud et al., 2015), and neuropathic pain (Bravo et al., 2014; Weaver et al., 2017; Mousseau et al., 2018). While pannexins have limited sequence identity with innexins (~15% identity), they have virtually no sequence similarity to other large-pore forming channels (Panchin et al., 2000). Among the pannexin family, pannexin 1 (Panx1) has garnered the most attention for its role as a large-pore forming channel responsible for ATP release from a variety of cell types (Bao et al., 2004; Dahl, 2015). Different kinds of stimuli have been reported to activate Panx1 including voltage, membrane stretch, increased intracellular calcium levels, and positive membrane potentials

2

41 (Bruzzone et al., 2003; Bao et al., 2004; Locovei et al., 2006; Wang et al., 2014; Chiu et al.,

42 2018). Panx1 is also targeted by signaling effectors, such as proteases and kinases, to

43 permanently or temporarily stimulate channel activity (Pelegrin and Surprenant, 2006;

44 Thompson et al., 2008; Sandilos et al., 2012; Billaud et al., 2015; Lohman et al., 2015). The

45 above evidence suggests that Panx1 has a capacity to integrate distinct stimuli into channel

46 activation leading to ATP release. Despite playing critical roles in a variety of biological

47 processes, a mechanistic understanding of pannexin function has been largely limited due to

48 the lack of a high-resolution structure. Here, we show the cryo-EM structure of Panx1, which

49 reveals the pattern of heptameric assembly, pore lining residues, important residues for ion

50 selection, and a putative carbenoxolone binding site.

51

52 **Results**

53 Structure determination and functional characterization

54 To identify a pannexin channel suitable for structure determination, we screened 34 pannexin

55 orthologues using Fluorescence Size Exclusion Chromatography (FSEC)(Kawate and Gouaux,

56 2006). Frog Panx1 (frPanx1; 66% identical to human, **Figure1-figure supplement 1**) displayed

57 high expression levels and remained monodisperse when solubilized in detergent, suggesting

58 high biochemical integrity. We further stabilized frPanx1 by truncating the C-terminus by 71

59 amino acids and by removing 24 amino acids from the intracellular loop between

60 transmembrane helices 2 and 3 (**Figure1-figure supplement 1**). This construct, dubbed

61 "frPanx-ΔLC", displayed high stability in detergents and could be purified to homogeneity

62 (**Figure1-figure supplement 2a and b**). We verified that frPanx1 forms a functional pannexin

63 channel by whole-cell patch clamp electrophysiology (**Fig.1a and b; Figure1-figure**

64 **supplement 2e and f**). Purified frPanx1-ΔLC was reconstituted into nanodiscs composed of

65 MSP2N2 (an engineered derivative of apolipoprotein) and soybean polar lipids, and subjected to

66 cryo-electron microscopy (cryo-EM) and single particle analysis (**Figure1-figure supplement**

67 **2c and d**). We used a total of 90,185 selected particles for 3D reconstruction at 3.0 Å resolution

68 (**Figure1-figure supplement 3**). The map quality was sufficient for *de novo* model building for

69 the majority of frPanx1-ΔLC with the exception of disordered segments of the N-terminus

70 (residues 1-10), ECL1 (88-100), and ICL1 (157-194) (**Fig. 1c; Figure1-figure supplement 4,**

71 **Video 1, and Table 1**).
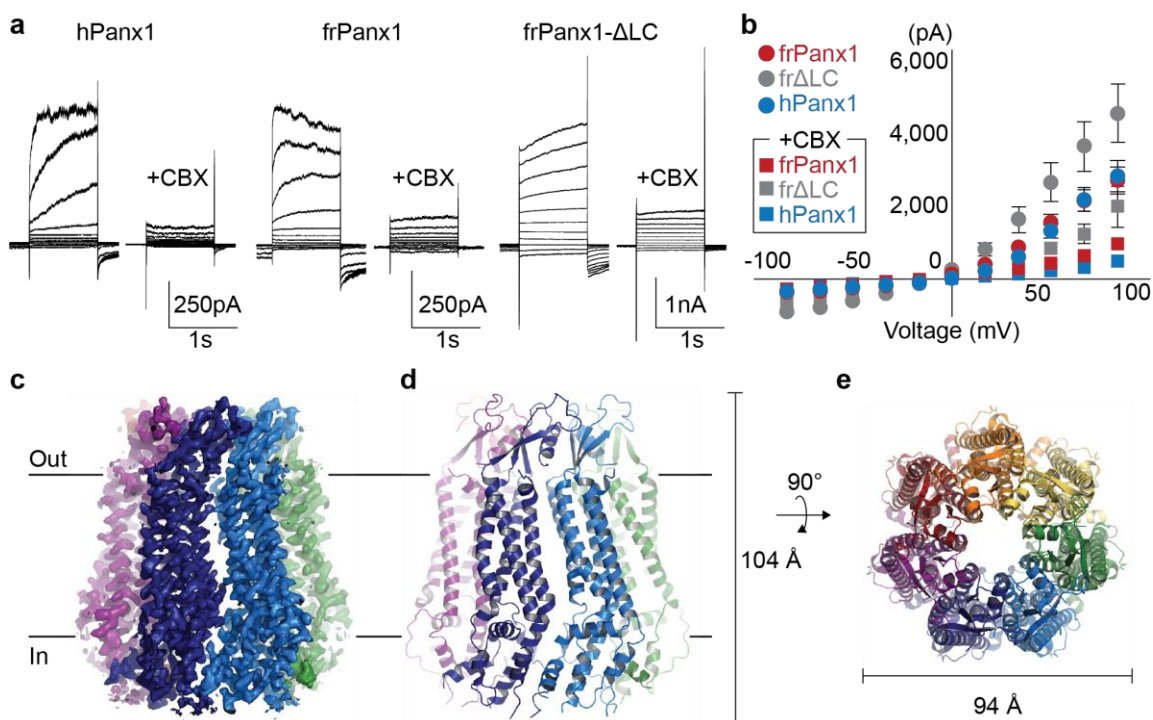
73 **Figure 1. frPanx1 forms a heptameric ion channel. a,** Whole-cell patch clamp recordings from HEK

74 293 cells expressing hPanx1, frPanx1, and frPanx1-ΔLC. Cells were clamped at -60 mV and stepped

75 from -100 mV to +100 mV for 1 s in 20 mV increments. To facilitate electrophysiological studies, we

76 inserted a Gly-Ser motif immediately after the start Met to enhance Panx1 channel opening as we have

77 previously described (Michalski et al., 2018). CBX (100 µM) was applied through a rapid solution

78 exchanger. **b,** Current-voltage plot of the same channels shown in **a**. Recordings performed in normal

79 external buffer are shown as circles, and those performed during CBX (100 µM) application are shown as

80 squares. Each point represents the mean of at least 3 different recordings, and error bars represent the

81 SEM. **c,** EM map of frPanx1-ΔLC shown from within the plane of the membrane. Each protomer is

82 colored differently, with the extracellular side designated as "out" and the intracellular side as "in." **d,**

83 Overall structure of frPanx1-ΔLC viewed from within the lipid bilayer. **e,** Structure of frPanx1 viewed from

84 the extracellular face.

85

86 <u>Overall structure and protomer features</u>

87 The frPanx1- ΔLC structure revealed a heptameric assembly, which is unique among the known

88 eukaryotic channels (**Fig. 1d and e**). Other large-pore forming channels include hexameric

89 connexins (Maeda et al., 2009) and LRRC8s (Deneka et al., 2018; Kasuya et al., 2018;

90 Kefauver et al., 2018), and the octameric innexins (Oshima et al., 2016) and calcium

91 homeostasis modulator (CALHM1) (Syrjanen et al., 2020) (**Figure2-figure supplement 1**). Our

92 result differs from previous studies that suggest hexameric assembly of pannexin based on

93 single channel recordings on concatemeric channel and negative stain electron microscopy

94 (Boassa et al., 2007; Wang et al., 2014; Chiu et al., 2017). The heptameric assembly observed

95 in the current study is unlikely to be caused by the carboxy-terminal truncation or intracellular

96 loop deletion because cryo-EM images of the full-length frPanx1 also display clear seven-fold

97 symmetry in the 2D class averages (**Figure2-figure supplement 2a**). Furthermore, 2D class

98 averages of hPanx1 display a heptameric assembly, but not other oligomeric states (**Figure2-**

99 **figure supplement 2b**). Thus, overall, our data suggests that the major oligomeric state of

100 Panx1 is a heptamer. This unique heptameric assembly is established by inter-subunit

101 interactions at three locations: 1) ECL1s and the loop between β2 and β3; 2) TM1-TM1 and

102 TM2-TM4 interfaces; and 3) α9 helix and the surrounding α3 and α4 helices, and the N-terminal

103 loop from the neighboring subunit (**Figure2-figure supplement 3**). Notably, the majority of

104 residues mediating these interactions are highly conserved (e.g. Phe67 and Tyr111; **Figure1-**

105 **figure supplement 1**).

106 The overall protomer structure of Panx1 resembles that of other large-pore forming

107 channels including connexin, innexins, and LRRC8. Like other large-pore forming channels,

108 each Panx1 protomer harbors four transmembrane helices (TM1-4), two extracellular loops

109   (ECL1 and 2), two intracellular loops (ICL1 and 2), and an amino (N)-terminal loop (**Fig. 2a and**

110   **b**). The transmembrane helices of Panx1 are assembled as a bundle in which the overall helix

111   lengths, angles, and positions strongly resemble the transmembrane arrangements observed in

112   other large-pore channels (**Fig. 2c**). In contrast, Panx1 has no similarity in transmembrane

113   arrangement to another group of large-pore channels, CALHMs whose protomers also contain

114   four transmembrane helices (Choi et al., 2019; Syrjanen et al., 2020) (**Figure2-figure**

115   **supplement 1**). Structural features in the Panx1 ECL1 and ECL2 domains are conserved

116   among large-pore channels despite limited sequence similarity (**Fig. 2d-g; Figure2-figure**

117   **supplement 1**). For example, the Panx1 ECL1 and ECL2 are joined together by two conserved

118   disulfide bonds (Cys66 with Cys267, Cys84 with Cys248) in addition to several β-strands. ECL1

119   also contains an alpha-helix that extends towards the central pore and forms an extracellular

120   constriction of the permeation pathway. While much of the transmembrane domains and

121   extracellular loops show similarities to other large-pore forming channels, the Panx1 intracellular

122   domains are structurally unique (**Figure2-figure supplement 1**). ICL1 and ICL2, for example,

123   together form a bundle of helices that make contact with the N-terminus. The N-terminal loop of

124   Panx1 forms a constriction of the permeation pathway and extends towards the intracellular

125   region. The first ~10 amino acids of the N-terminus are disordered in our structure, but these

126   residues might play a role in ion permeation or ion selectivity (Wang and Dahl, 2010).

127

6
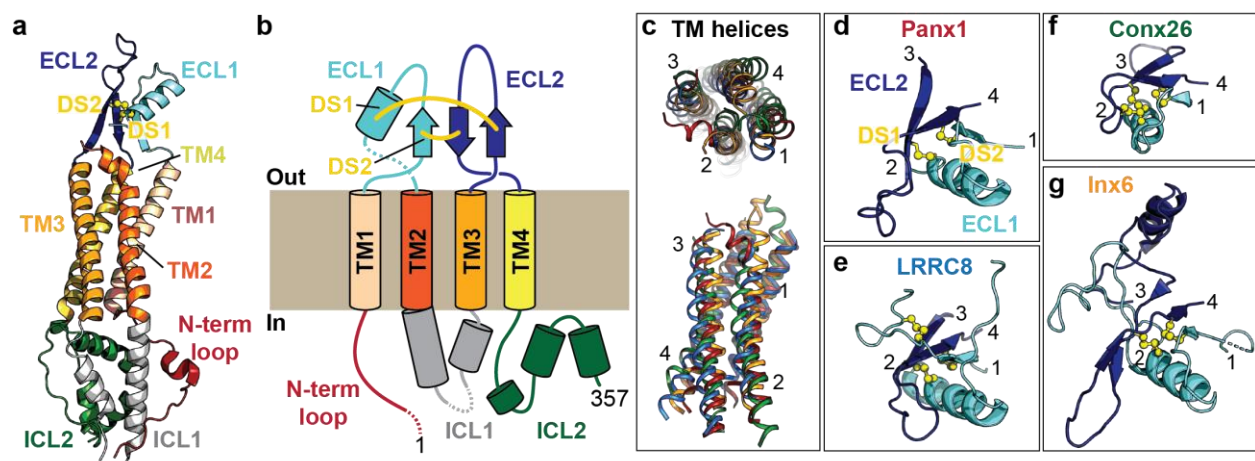
128 **Figure 2. Subunit architecture of frPanx1. a,** Structure of the frPanx1 protomer. Each domain is colored

129 according to the cartoon scheme presented in **b**. **c.** Superimposition of the transmembrane helices from

130 frPanx1 (red), connexin-26 (green), innexin-6 (orange), and LRRC8 (blue) shown top-down from the

131 extracellular side (top) or from within the plane of the membrane (bottom). **d-g,** Cartoon representation of

132 the extracellular loops of large pore forming channels. ECL1 is colored in light blue, and ECL2 is colored

133 in dark blue, and disulfide bridges are shown as yellow spheres. These domains are viewed from the

134 same angle (from top) as shown in the top panel in **c**.

135

136 <u>Ion permeation pathway and selectivity</u>

137 The Panx1 permeation pathway spans a length of 104 Å, with constrictions formed by the N-

138 terminal loop, Ile58, and Trp74 (**Fig. 3a and b**). The narrowest constriction is surrounded by

139 Trp74 located on ECL1 (**Fig. 3c**). Trp74 is highly conserved among species including hPanx1

140 (**Figure1-figure supplement 1**). Because Panx1 has been previously characterized as an

141 anion selective channel (Ma et al., 2012; Romanov et al., 2012; Chiu et al., 2014), we wondered

142 if positively charged amino acids around the narrowest constriction formed by Trp74 may

143 contribute to anion selectivity of the channel. Interestingly, Arg75 is situated nearest to the

144 tightest constriction of the permeation pathway (**Fig. 3d**). We hypothesized that Arg75 might be

145 a major determinant of anion selectivity of Panx1 channels in the open state. To assess whether

146 Arg75 contributes to anion selectivity, we generated a series of point mutations at this position

147 on hPanx1 and compared their reversal potentials (Erev) in asymmetric solutions using whole-

148 cell patch clamp electrophysiology (**Fig. 3e and Figure3-figure supplement 1**). We kept

149 sodium chloride (NaCl) constant in the pipette solution while varying the extracellular solution.

150 When treated with the large anion, gluconate (Gluc$^-$), Erev shifted to +26 mV, suggesting the

151 channel is more permeable to Cl$^-$ than to Gluc$^-$. When exposed to the large cation, *N*-methyl-D-

152 glucamine (NMDG$^+$), Erev remained close to 0 mV, suggesting that Na$^+$ and NMDG$^+$ equally (or

153 do not) permeate Panx1. These results are consistent with Panx1 being an anion-selective

154   channel. The Arg75Lys mutant maintains the positive charge of this position, and displayed

155   Erev values comparable to WT. Removing the positive charge at this position, as shown by the

156   Arg75Ala mutant, diminished Cl$^-$ selectivity as the Erev in NaGluc remained near 0 mV.

157   Interestingly, the Erev in NMDGCl shifted to -22 mV, suggesting the channel had lost anion

158   selectivity and Na$^+$ became more permeable than NMDG$^+$. A charge reversal mutant, Arg75Glu,

159   shifted the Erev in NaGluc to -16 mV and in NMDGCl to -45 mV, indicating that Gluc$^-$ became

160   more permeable to Cl$^-$. Overall, these results support the idea that the positively charged Arg75

161   plays a role in anion selectivity of Panx1.

162   We next wondered if introducing a charge at position 74 might alter ion selectivity of

163   Panx1 channels. Interestingly, both Trp74Arg and Trp74Glu mutants become less selective to

164   anions and more permeable to Na$^+$ (**Figure 3e**). These results suggest that introducing a charge

165   at this position disrupts the natural ion selectivity of Panx1 channels but that position 74 itself

166   does not control ion selectivity. We observed that the distance between the guanidyl group of

167   Arg75 and the benzene ring of Trp74 from an adjacent subunit is ~4 Å, suggesting that these

168   two residues likely participate in an inter-subunit cation-π interaction key to Panx1 ion selectivity

169   (**Figure 3f**). To test this hypothesis, we generated Trp74Ala and Trp74Phe mutations and

170   measured Erev potentials. Trp74Ala showed a marked decrease in Cl$^-$ permeability and an

171   increase in Na$^+$ permeability, despite preservation of the positive charge at Arg75. A more

172   conservative mutation, Trp74Phe, still disrupted ion selectivity, suggesting that proper

173   positioning of the benzene ring at position 74 is important for anion selection. Altogether, our

174   data suggests that anion selectivity is only achieved when Trp74 and Arg75 form a cation-π

175   interaction. Given that our structure has disordered and truncated regions in the N-terminus,

176   ICL1, and ICL2, it is possible that additional ion selectivity or gating regions exist in the full-

177   length channel. For example, the N-termini of LRRC8 and connexins perform an important role

178   in ion selectivity (Kyle et al., 2008; Kronengold et al., 2012; Kefauver et al., 2018). It is possible

179   that the N-terminus of Panx1 is mobile and may further constrict the permeation pathway.

180　Another possibility is that the electrostatic potential along the pore pathway contributes to the

181　ion selectivity. Interestingly, both cytoplasmic and extracellular entrances of the permeation

182　pathway are mostly basic, suggesting that non-permeant cations may be excluded from the

183　pore (**Figure3-figure supplement 2**). In contrast, the region underneath the W74 constriction is

184　highly acidic, supporting the idea that anions may be selected around this area.

185
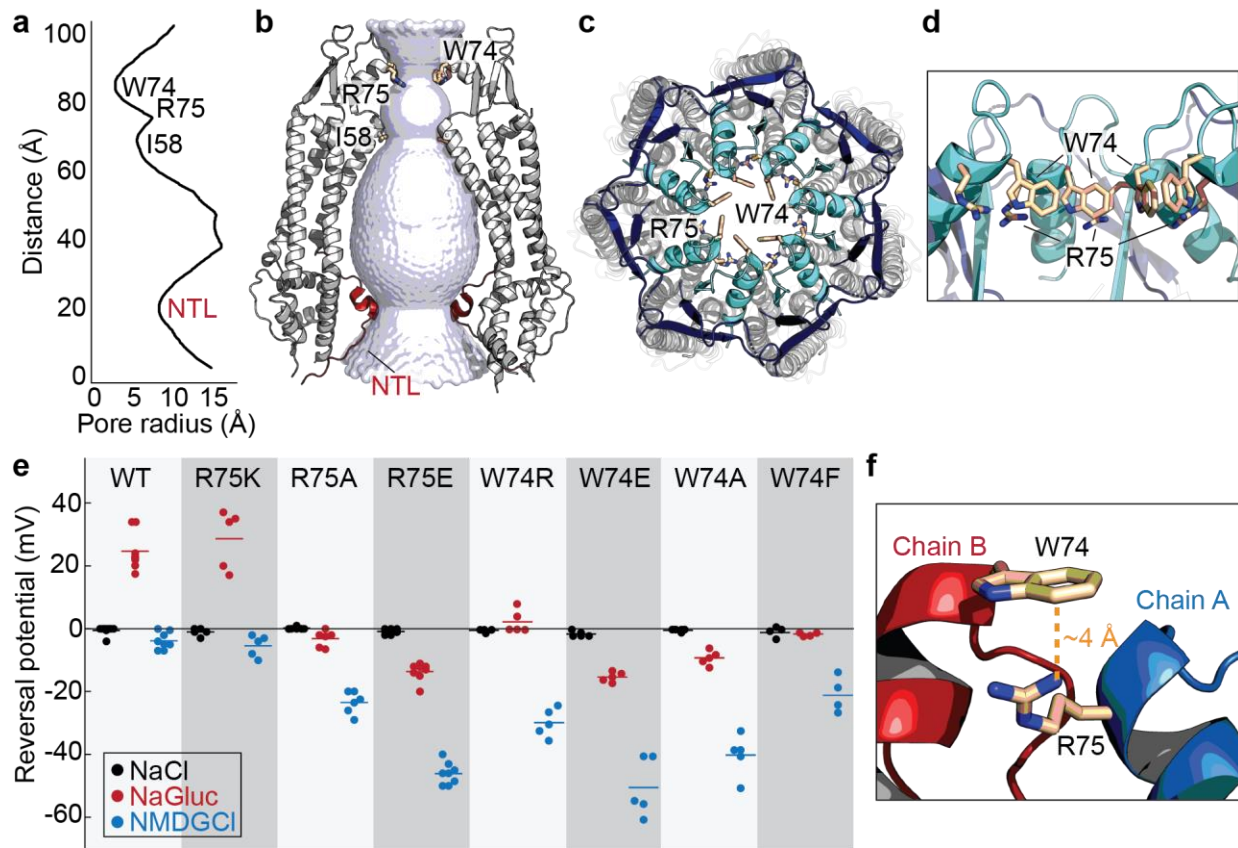
186

187　**Figure 3. Permeation and ion selectivity of Panx1 channels. a,** HOLE (Smart et al., 1996) diagram

188　demonstrating constrictions along the permeation pathway. NTL; N-terminal loop. **b,** Surface

189　representation of the internal space along the molecular 7-fold axis running through the center of frPanx1.

190　The surface was generate using HOLE. **c and d,** Top view facing the extracellular side (**c**) or side view

191　(**d**) of frPanx1, with ECL1 shown in light blue and ECL2 in dark blue. Trp74 and Arg75 are shown as

192　sticks. **e,** Reversal potentials of various hPanx1 ion selectivity mutants. Each point represents the Erev

193　measured in NaCl (black), NaGluc (red), or NMDGCl (blue), and bars represent the mean values. I-V

194   curves were obtained by a ramp protocol from -80 mV to +80 mV. **f,** Close-up view of the Trp74-Arg75

195   interaction at the interface of protomer A (blue) and B (red).

196

197   <u>CBX action mechanism</u>

198   We have previously demonstrated that CBX, a potent nonselective inhibitor of Panx1, likely acts

199   through a mechanism involving ECL1 (Michalski and Kawate, 2016). In these experiments,

200   mutations at a number of residues in ECL1 rendered Panx1 less sensitive to CBX-mediated

201   channel inhibition. Mapping such residues in the Panx1 structure revealed that they are

202   clustered proximal to the extracellular constriction by Trp74, in a groove formed between ECL1

203   and ECL2 (**Figure 4a and b**). This supports our previous speculation that CBX is an allosteric

204   inhibitor, not a channel blocker (Michalski and Kawate, 2016).

205   Given that this hydrophobic groove is formed also by residues in ECL2, we wondered if

206   residues in ECL2 might also play a role in CBX-mediated inhibition. We mutated selected

207   residues in ECL2 of hPanx1 to cysteines and measured channel activity before and after CBX

208   application. We found that mutations at Ile247, Val258, and Phe262 (hPanx1 numbering)

209   diminished CBX-sensitivity (**Figure 4b**). These data suggest that both ECL1 and ECL2 play

210   important roles in inhibition of Panx1 by CBX. Although we do not have a cryo-EM structure

211   complexed to CBX at this point, we speculate that CBX inhibits Panx channels by binding

212   between ECL1 and ECL2 and 'locking' the conformation of gate forming ECL1 in favor of

213   channel closure.

214
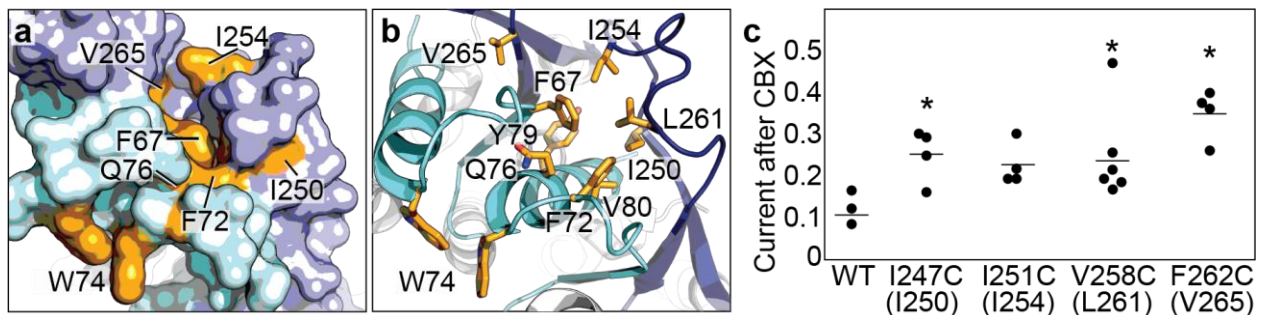
215 **Figure 4. CBX action requires residues from both ECL1 and ECL2. a and b,** Surface (**a**) and cartoon

216 (**b**) representations of the frPanx1 ECL1 (light blue) and ECL2 (dark blue), with potential CBX-interacting

217 residues shown in orange. **c,** Quantification of whole-cell currents from hPanx1 mutants when treated

218 with CBX (100 μM). Mutants are numbered according to the hPanx1 sequence while the mutants in

219 parenthesis are the corresponding residues in frPanx1. Recordings were performed by stepping to +100

220 mV in the absence or presence of CBX, and each point represents the normalized current amplitude

221 during the CBX application. Bars represent the mean value from each mutant. Asterisks indicate

222 significance of $p<0.05$ determined by one-way ANOVA followed by Dunnett's test comparing WT to each

223 mutant (F262C: $p=0.0007$; I247C: $p=0.0471$; V258C: $p=0.0363$).

224

225 **Discussion**

226 The frPanx1-ΔLC structure uncovered a unique heptameric assembly of a large-pore channel

227 that harbors an extracellular constriction formed by Trp74 and Arg75. These residues are

228 located on ECL1 and face toward the central pore of the channel and thus, are situated to

229 regulate channel function. Mutagenesis studies at these positions revealed that both residues

230 play pivotal roles in ion selection. Unlike the LRRC8A anion channel, however, the positively

231 charged Arg75 does not seem to form a canonical selectivity filter. Instead, the guanidinium

232 group of Arg75 likely mediates a cation-π interaction with Trp74 in the neighboring subunit,

233 which seems to control ion selection. One possible ion selection mechanism is that this cation-π

234 interactions stabilize the inter-subunit interactions, which in turn creates an electrostatic

235 environment that favors anion permeation. Another possibility is that tight inter-subunit

236 interactions in the extracellular domain is necessary to form an ion selectivity filter in the missing

237 region in our current model (e.g. N-terminus or C-terminal domain).

238   Which functional state does our model represent? Based on the lack of channel activity

239 at 0 mV (**Figure1-figure supplement 2e and f)**, our current structure may represent a closed

240 conformation. This is supported by the existence of a highly acidic region near Trp74 (**Figure3-**

241 **figure supplement 2**), which may serve as a barrier for anions to permeate. However, given

242 that the narrowest constriction at Trp74 is ~10 Å wide, it is possible that the structure actually

243 represents an open conformation. Indeed, the +GS version of frPanx1-ΔLC shows larger leak

244 currents (**Figure 1a and b**), suggesting that the C-terminal truncation may promote channel

245 opening while lack of the N-terminal modification renders it closed. If the conformation of the N-

246 terminus in frPanx1-ΔLC is somehow compromised during purification or reconstitution into

247 nanodiscs, it is possible that our structure may actually look closer to the +GS version. While

248 further studies are necessary to define the functional state of our current structure, the weak EM

249 density in the N-terminal region leaves the possibility that frPanx1-ΔLC may be representing an

250 open state.

251   We found that ECL1 and ECL2 interact to each other and form a potential CBX binding

252 pocket. Both ECL1 and ECL2 may undergo movement based on conformational alterations of

253 the TMDs and cytoplasmic domains. For example, it is conceivable that movement of the TMDs

254 caused by membrane stretch or voltage, or changes in the cytoplasmic domain triggered by

255 caspase cleavage may be coupled to conformational rearrangements in the extracellular

256 domain. The major role of the extracellular domain in pannexin function is strongly supported by

257 our experimental results demonstrating that mutating Trp74 and Arg75, as well as surrounding

258 residues in ECL1 and ECL2, alter channel properties including ion selectivity. Furthermore, we

259 previously demonstrated that application of CBX to mutants at Trp74 (e.g. to Ala, Ile, Lys)

260 potentiates voltage-dependent channel activity (Michalski and Kawate, 2016), which indicates

261 that CBX likely acts as an allosteric inhibitor rather than a channel blocker.

262   In contrast to the extracellular domain, roles of the intracellular domain remain elusive.

263 While the C-terminal domain has been demonstrated to play important roles in Panx1 channel

264 gating (Sandilos et al., 2012), our study neither confirms or refutes this mechanism as half of

265 this domain is missing in our current structure. Likewise, the first 10 residues in the N-terminus

266 are disordered, making it challenging to understand how these residues tune the activity of

267   Panx1 channel (Michalski et al., 2018). Given their important roles in channel gating, it is

268   possible that the unmodeled N-terminal region may interact with the deleted region of the C-

269   terminal domain. It is also possible that these domains may form a channel gate. In contrast to

270   these domains, the deleted residues in ICL-1 (between Gly171 and Lys194) seems to play a

271   minimal role in channel gating. We surveyed 23 different deletion constructs (in which each

272   variant harbored a different deletion length and position) and among these, all deletions

273   constructs showed voltage-dependent channel activity via whole-cell patch clamp, with the

274   exception of a construct in which the entire region between Lys155 and Lys194 was removed.

275   We also tested these deletion constructs using FSEC and found that all functional constructs

276   were properly assembled into heptamers. The above evidence indicates that the deleted region

277   in ILC-1 plays an insignificant role in channel gating. The EM density in this region was weak

278   and could not be modelled, indicating a high degree of conformational flexibility.

279   In conclusion, our frPanx1-ΔLC structure provides an important atomic blueprint for

280   dissecting functional mechanisms of Panx1. While we did not observe a gate-like structure in

281   the current cryo-EM map, the missing domains, especially the N-terminal loop and the C-

282   terminal domain, may serve as a channel gate on the intracellular side of the channel. Further

283   structure-based experiments such as cysteine accessibility and molecular dynamics simulations

284   will facilitate our understanding of how this unique large-pore channel functions.

285

286

Figure supplements and Table
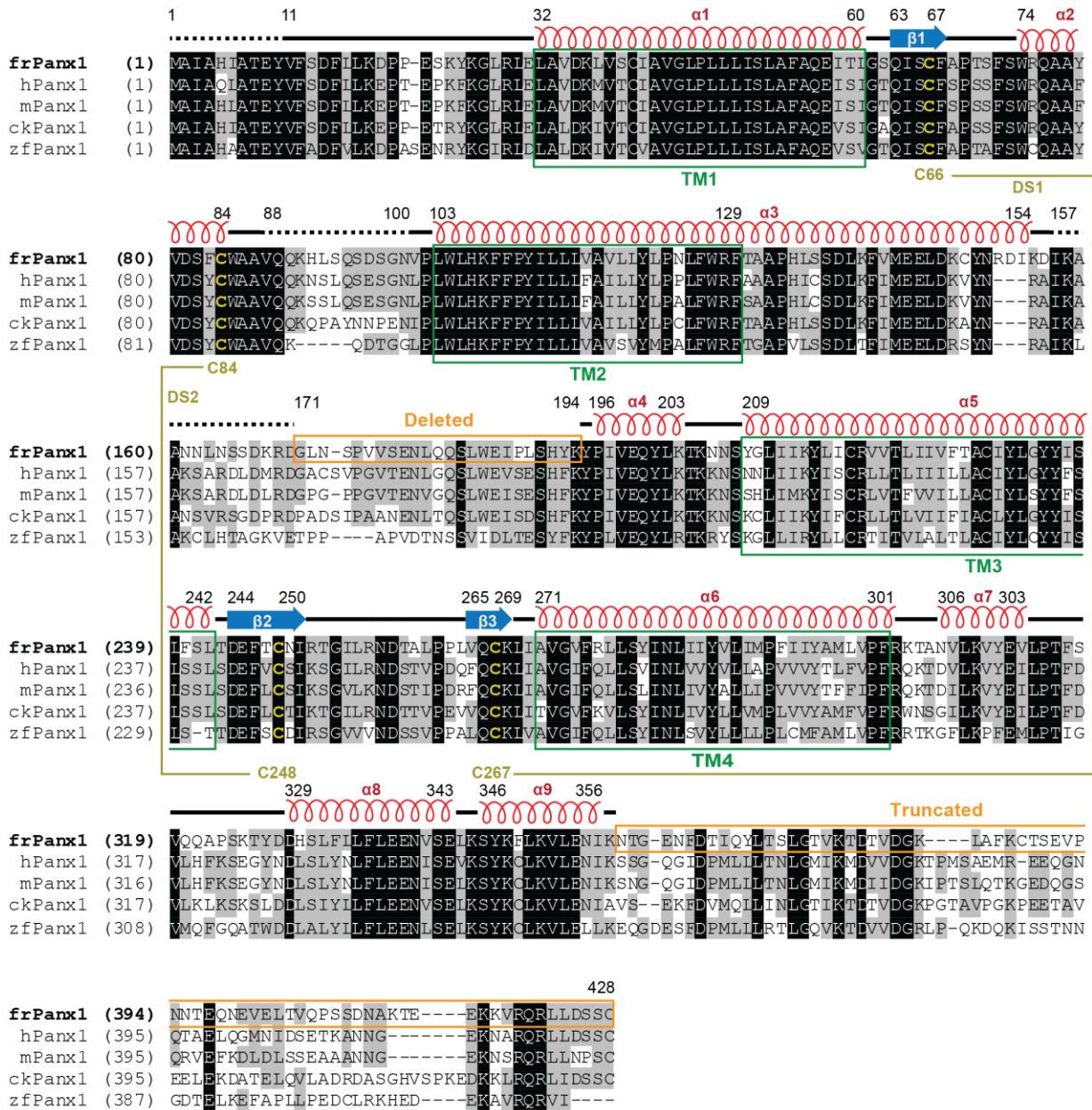
Figure1-figure supplement 1. Sequence alignment and structural features. Amino acid sequence of frPanx1 compared to various Panx1 orthologues. Amino acids highlighted in black are completely conserved, in grey are similar, and in white are not conserved. Disulfide-forming cysteines are highlighted in yellow. Secondary structure features are shown above the sequence alignment. Green boxes depict the transmembrane helix boundaries, and orange boxes show deleted or truncated regions to create frPanx1-ΔLC.

295
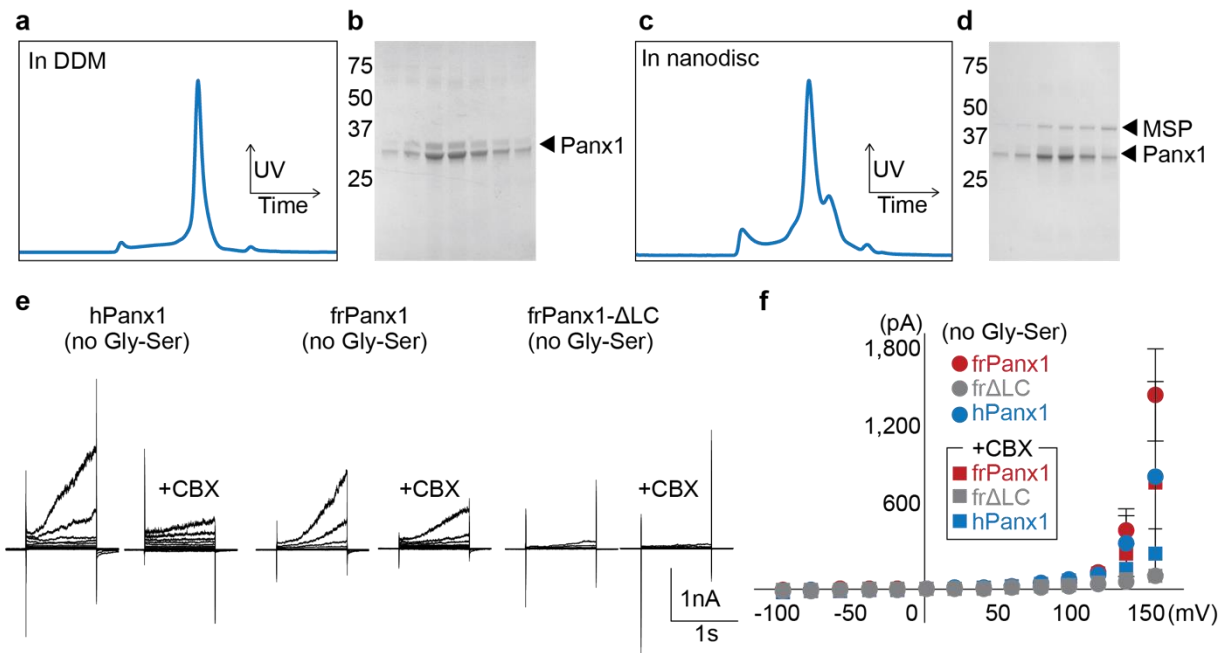
Figure1-figure supplement 2. Characterization of frPanx1-ΔLC. **a,** Size exclusion chromatogram of
frPanx1-ΔLC. Concentrated protein was injected onto a Superose 6 10/300 column equilibrated with 150
mM NaCl, 10 mM Tris pH 8.0, 1 mM EDTA, 0.5 mM DDM. **b,** SDS-PAGE analysis of peak fractions
collected from **a**. **c,** Size exclusion chromatogram of frPanx1-ΔLC after reconstitution into nanodiscs. The
running buffer contained 150 mM NaCl, 10 mM Tris pH 8.0, 1 mM EDTA. **d,** SDS-PAGE analysis of peak
fractions collected from **c**. **e,** Whole-cell recordings of wild-type (no Gly-Ser) hPanx1, frPanx1, and
frPanx1-ΔLC. Whole-cell patches from transfected HEK 293T cells were obtained, held at -60 mV, and
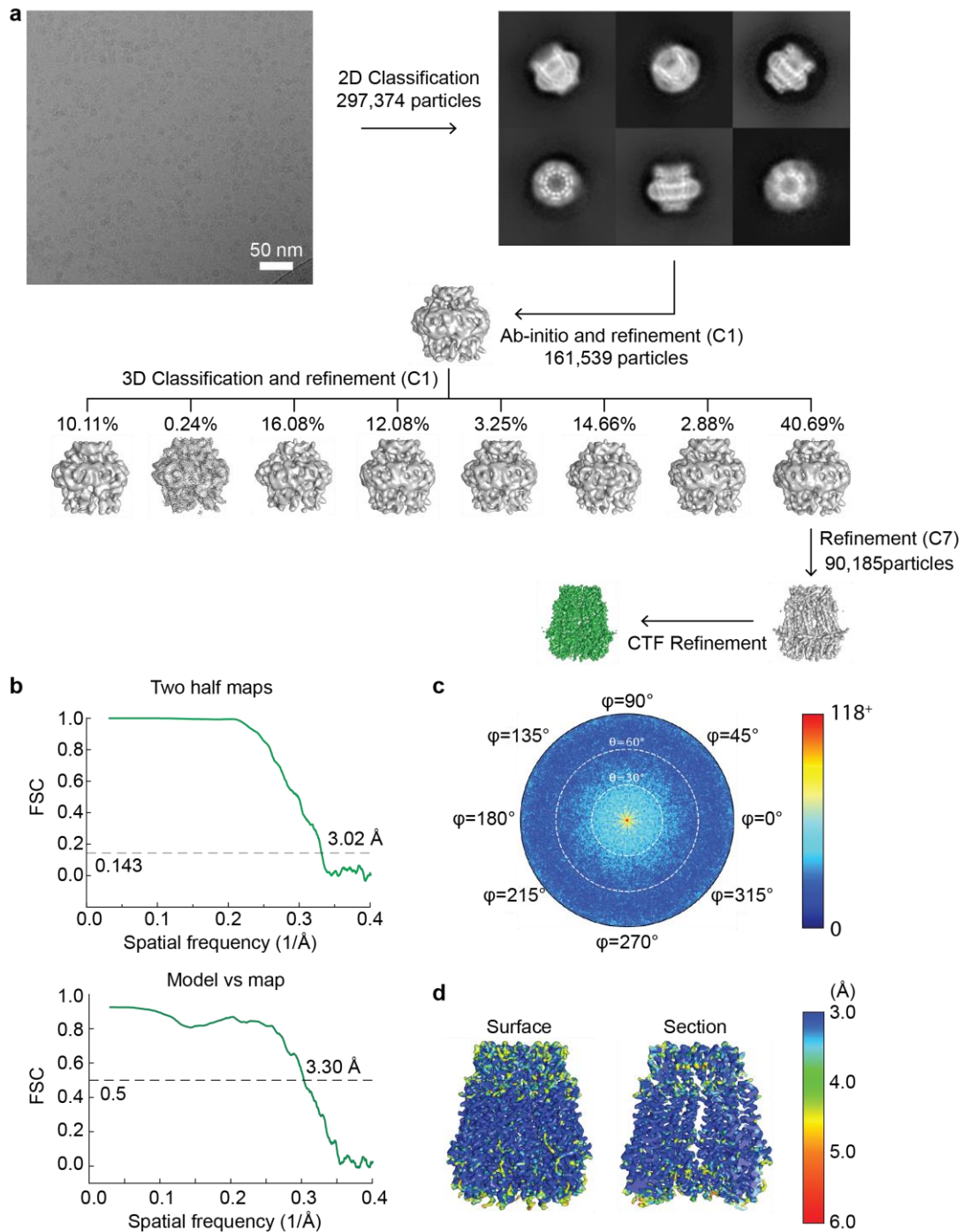stepped between -100 mV and +160 mV for 1 s. CBX (100 µM) was applied through a rapid solution
exchanger. **f,** Current-voltage plot of wild-type pannexin recordings shown in **e**. Each circle represents the
mean current at a particular voltage, with squares depicting the same current when treated with 100 µM
CBX. N=3-11.

307

308

309
Figure1-figure supplement 3. Cryo-EM image processing workflow for single particle analysis of

frPanx1-ΔLC a. A representative micrograph (scale bar = 50 nm), representative 2D class averages, and

the 3D classification workflow are shown. **b.** The FSC plots of the two half maps (top) and the map vs

model (bottom) are shown. **c.** The angular distribution plot for class 3. **d.** Local resolutions of class 3 were

calculated using ResMap (Kucukelbir et al., 2014).

315
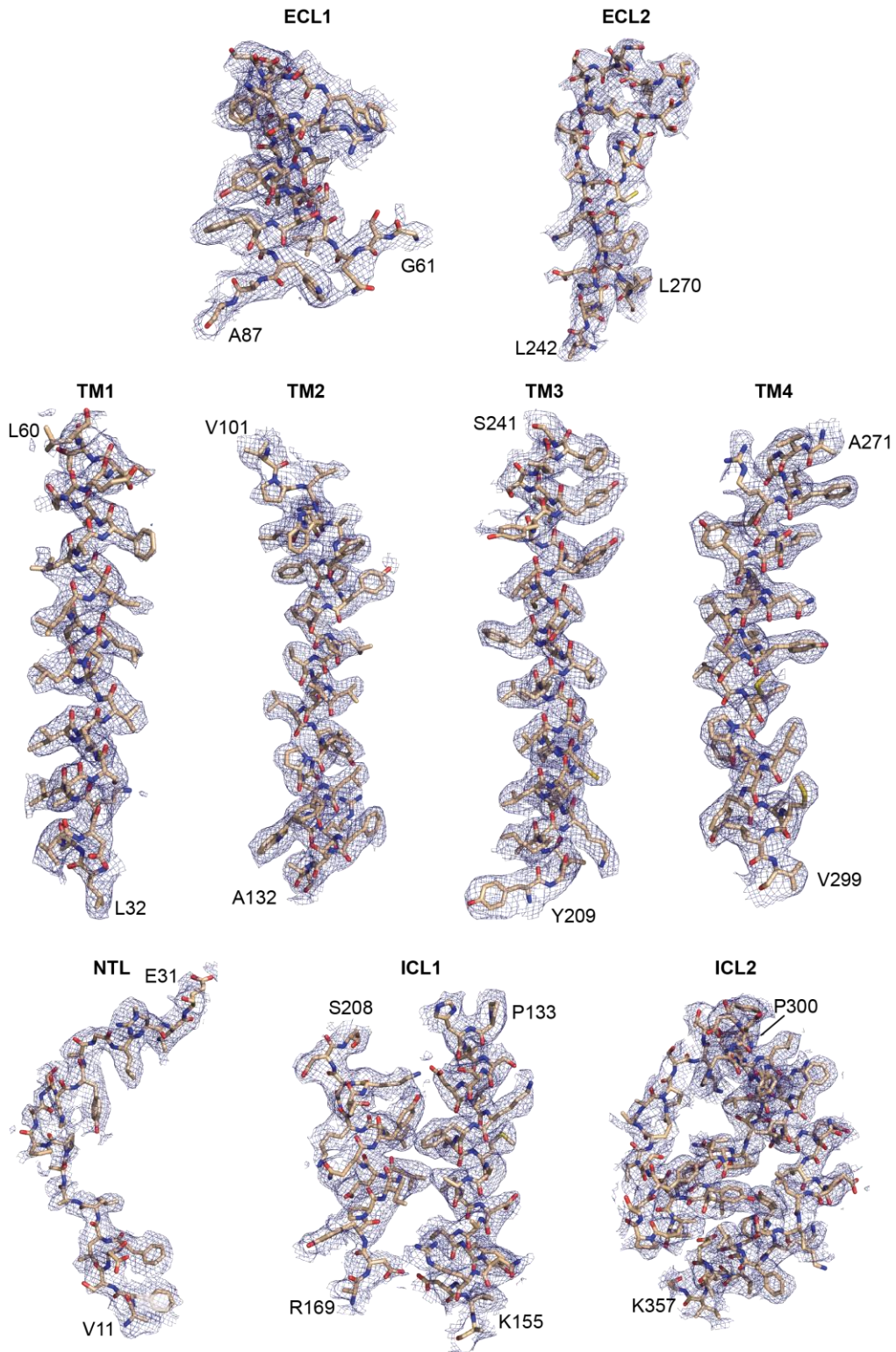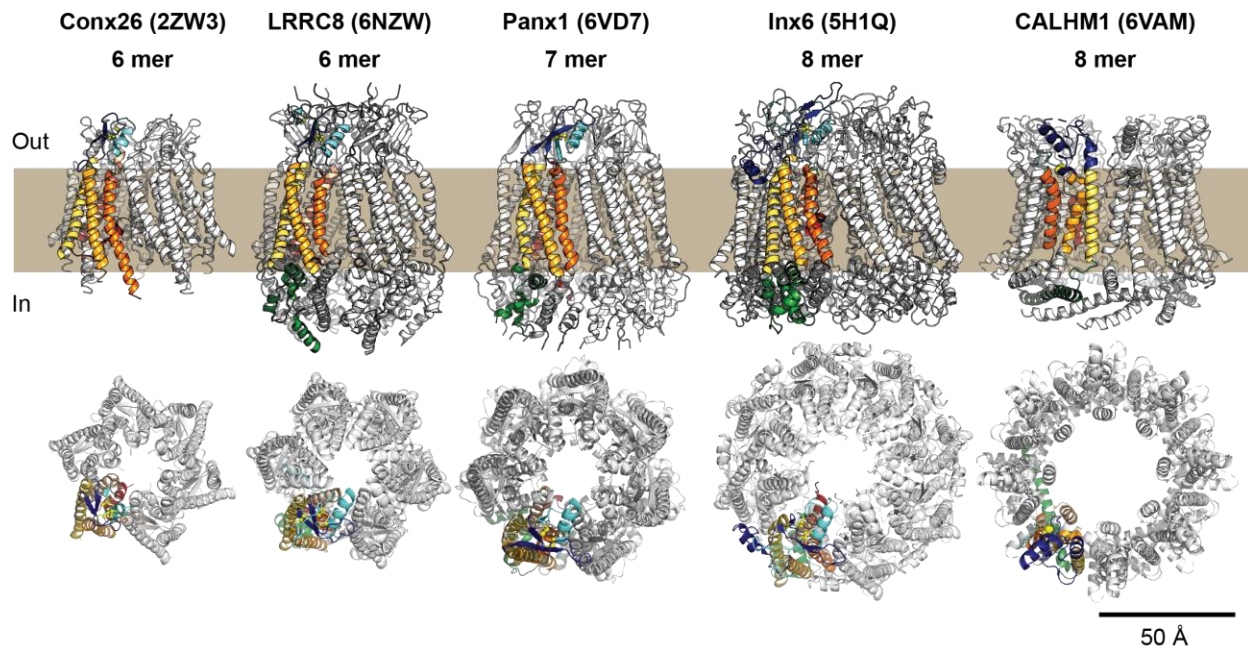
Figure1-figure supplement 4. Representative cryo-EM density of frPanx1-ΔLC. Each domain is shown as stick representation and fit into the corresponding density contoured at σ=3.0.

17

318

319

320

321 **Figure2-figure supplement 1. Comparison of frPanx1 with other large pore channels.** The structures

322 of connexin-26 (PDB: 2ZW3), LRRC8 (PDB: 6NZW), Panx1, innexin-6 (PDB: 5H1Q), and CALHM1 (PDB:

323 6VAM) are shown from within the plane of the membrane (top) and viewed from the extracellular side

324 (bottom). One subunit of each channel is shown colored with transmembrane domains in orange/yellow,

325 ECL1 is colored in light blue, ECL2 in dark blue, ICL1 in grey, ICL2 in green, and NTL in red, as shown in
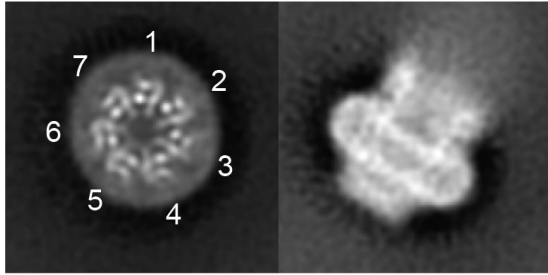
326 Fig. 2a.

327

328

329

330

331

332

333

a frPanx1-FL

b hPanx1-FL
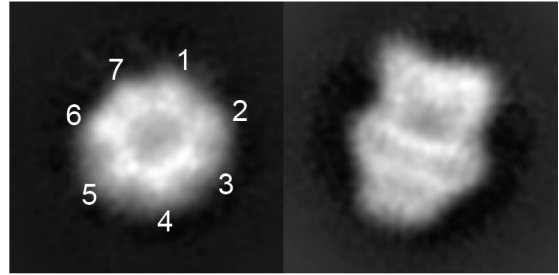
334
335

336 **Figure2-figure supplement 2. 2D classes of full-length frog and human pannexin 1. a**. 2D classes of

337 the full-length frog pannexin1 in nanodiscs showing top (left) and side (right) views. All seven protomers

338 are labeled with numbers in the 2D class of the top view. **b.** 2D classes of the full-length human pannexin

339 1 in DDM in the similar orientation to *panel a*. The top view shows a heptameric assembly (numbered).

340 No symmetry was imposed in 2D classification.

341
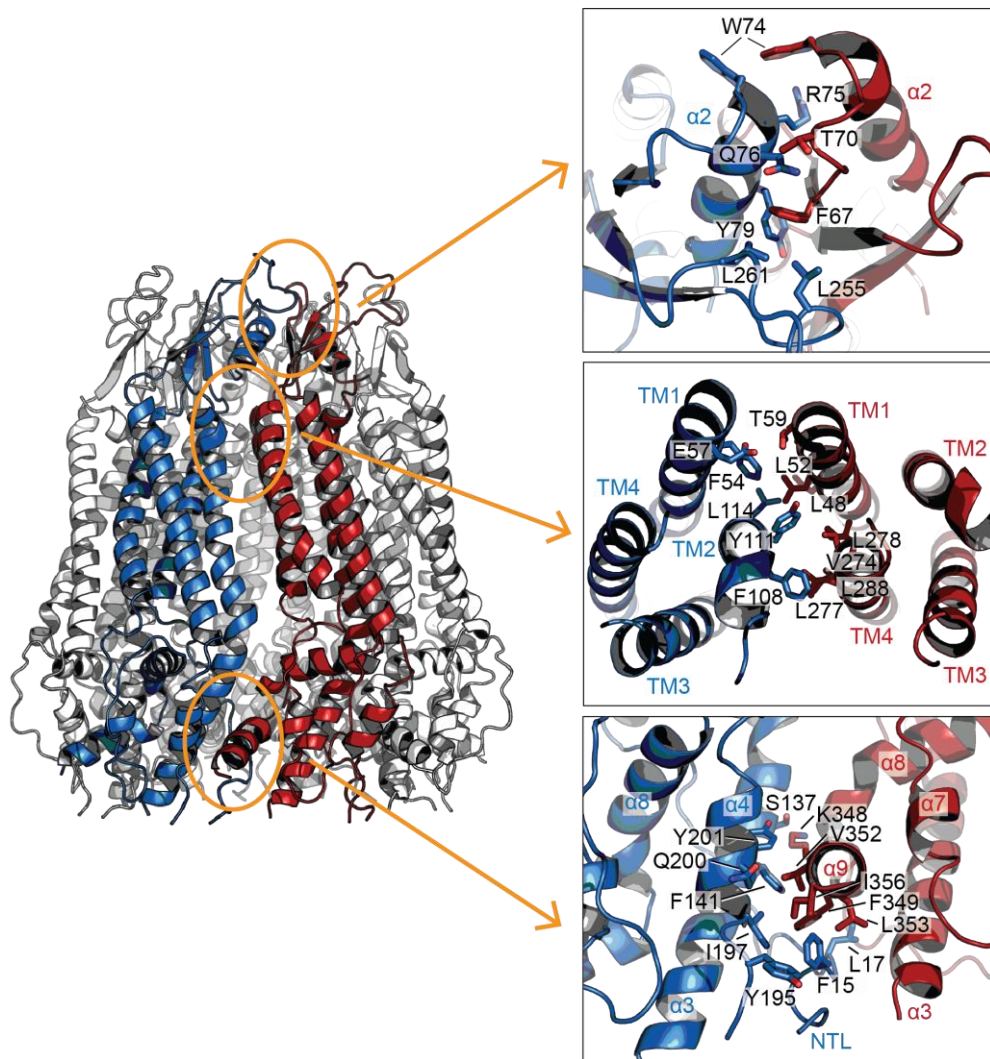
Figure2-figure supplement 3. Inter-subunit interactions. Three major inter-subunit interfaces between

two neighboring subunits (blue and red) are highlighted in orange ovals (left). Close-up views (right) show

the highly-conserved residues mediating the inter-subunit interactions.

345
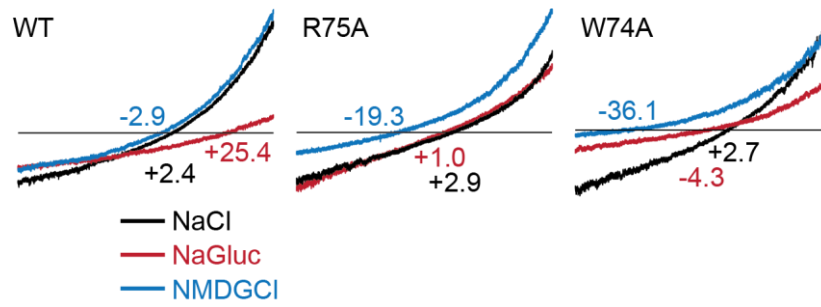
Figure3-figure supplement 1. Representative traces of the ramp recordings. HEK293 cells were held at -60 mV and ramped between -100 mV and + 100 mV over 3s duration. The numbers indicate the reversal potentials in mV.

349

350

351
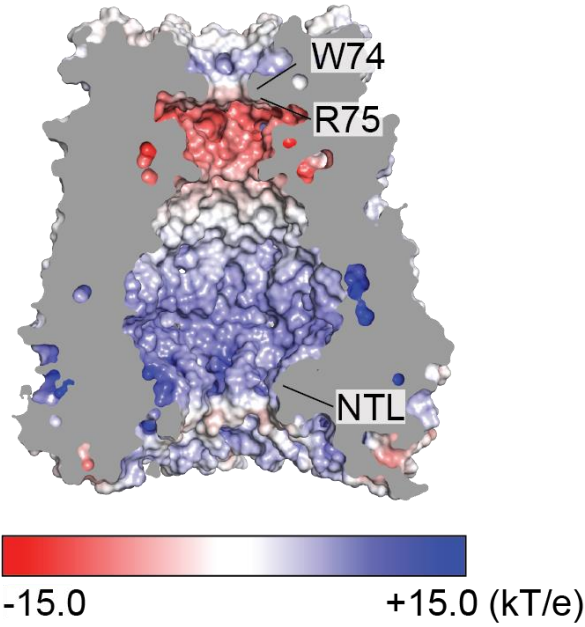
Figure3-figure supplement 2. Electrostatic surface potential of the ion permeation pathway. A

coronal section of frPanx1-ΔLC shows the surface of the ion permeation pathway. Electrostatic surface

potential was calculated using APBS plugin (Baker et al., 2001) in Pymol (Schrodinger, 2015) and

presented in the range between -15 kT/e (red: acidic) and +15 kT/e (blue: basic).

356

357

358 **Table 1. Cryo-EM data collection, refinement and validation statistics**

	frPanx- ΔLC (EMD-21150) (PDB: 6VD7)
Data collection and processing	
Magnification	130,000
Voltage (kV)	300
Electron exposure (e–/Å^2)	57.2
Defocus range (µm)	1.2-2.8
Pixel size (Å)	1.07
Symmetry imposed	C7
Initial particle images (no.)	297374
Final particle images (no.)	90185
Map resolution (Å)	3.02
FSC threshold	0.143
Refinement	
Initial model used (PDB code)	*de novo*
Model resolution (Å)	3.29
FSC threshold	0.5
Model resolution range (Å)	3-6
Map sharpening *B* factor (Å^2)	-90
Model composition	
Non-hydrogen atoms	16506
Protein residues	2079
Ligands	0
CC map vs. model (%)	0.85
R.m.s. deviations	
Bond lengths (Å)	0.008
Bond angles (°)	0.759
Validation	
MolProbity score	1.92
Clashscore	5.96
Poor rotamers (%)	0.78
Ramachandran plot	
Favored (%)	88.32
Allowed (%)	11.68
Disallowed (%)	0

359
360

361
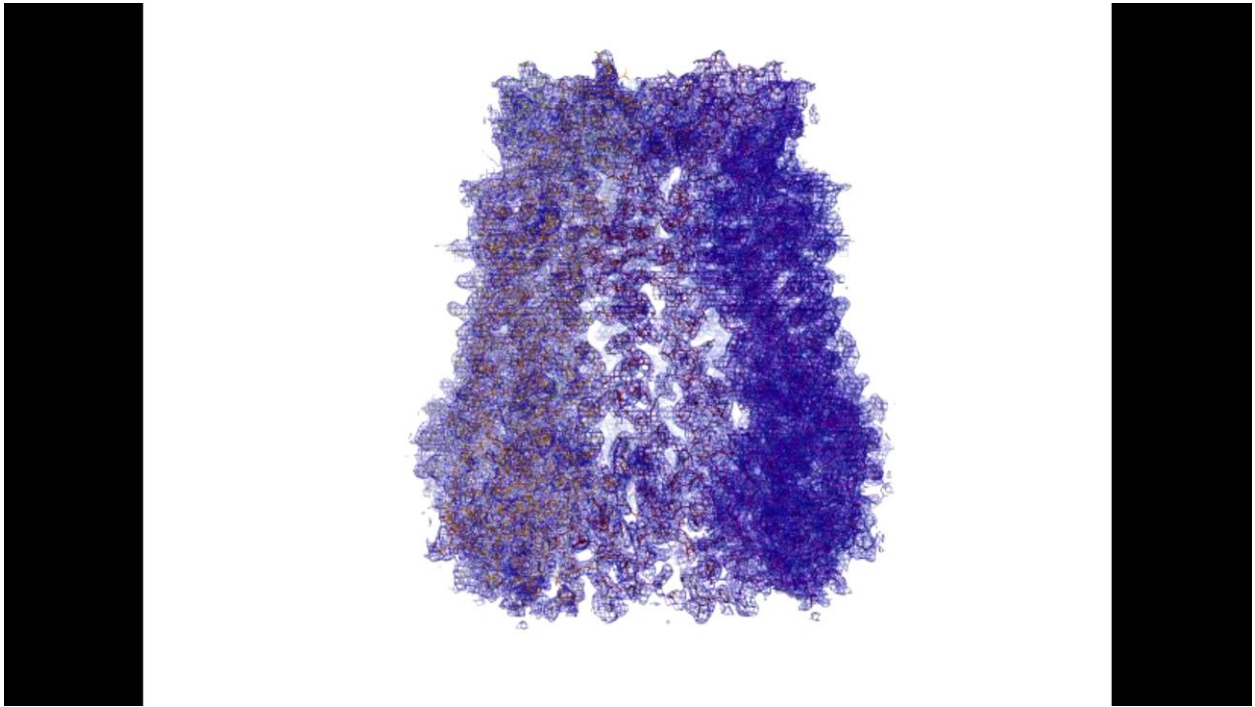
362
363 **Video 1. Cryo-EM density of frPanx1-ΔLC.** The model is shown as wire representation and fit into the
364 corresponding density contoured at σ=3.0. Each domain is colored differently and Tryp74 and Arg75 are
365 labeled in the close-up view.
366

367 **Materials and Methods**

Key Resources Table

Reagent type (species) or resource	Designation	Source or reference	Identifiers	Additional information
gene (*Xenopus tropicalis*)	frPanx1	Synthesized by Genscript	NCBI Reference Sequence: NP_001123728.1	Frog pannexin-1 gene sequence
gene (*Homo sapiens*)	hPanx1	Synthesized by Genscript	NCBI Reference Sequence: NP_056183.2	Human pannexin-1 gene sequence
cell line (*Homo sapiens*)	HEK293T cells	ATCC	Cat#: CRL-3216, RRID: CVCL_0045	
cell line (*Spodoptera frugiperda*)	Sf9 cells	ATCC	Cat#: CRL-1711, RRID: CVCL_0549	
recombinant DNA reagent	pIE2 hPanx1	doi: 10.1085/jgp.201711804		Mammalian expression vector for electrophysiology presented in Fig. 1 S2
recombinant DNA reagent	pIE2 hPanx1 +GS	doi: 10.1085/jgp.201711804		Mammalian expression vector for electrophysiology presented in Fig. 1, 3, and 4
recombinant DNA reagent	pIE2 frPanx1	This paper		Mammalian expression vector for electrophysiology presented in Fig. 1 S2
recombinant DNA reagent	pIE2 frPanx1 +GS	This paper		Mammalian expression vector for electrophysiology presented in Fig. 1
recombinant DNA reagent	pIE2 frPanx1-ΔLC	This paper		Mammalian expression vector for electrophysiology presented in Fig. 1 S2
recombinant DNA reagent	pIE2 frPanx1-ΔLC +GS	This paper		Mammalian expression vector for electrophysiology presented in Fig. 1
recombinant DNA reagent	pC-NG-FB7 frPanx1-ΔLC	This paper		Insect cell / baculovirus expression construct
recombinant DNA reagent	pC-NG-FB7 frPanx1	This paper		Insect cell / baculovirus expression construct
recombinant DNA reagent	pC-NG-FB7 hPanx1	This paper		Insect cell / baculovirus expression construct
peptide, recombinant protein	MSP2N2	doi: 10.1016/S0076-6879(09)64011-8		nanodisc expression construct

commercial assay or kit	Fugene 6	Promega	Cat#: E2691	
chemical compound, drug	Carbenoxolone	Sigma	Cat#: C4790	
chemical compound, drug	C12E8	Anatrace	Cat#: APO128	
chemical compound, drug	DDM	Anatrace	Cat#: D310	
chemical compound, drug	Soybean polar lipid extract	Avanti	Cat#: 541602	
software, algorithm	cisTEM	doi: 10.7554/eLife.35383	RRID: SCR_016502	
software, algorithm	Warp	doi: 10.1038/s41592-019-0580-y		
software, algorithm	Coot	doi: 10.1107/S0907444904019158	RRID: SCR_014222	
software, algorithm	PHENIX	doi: 10.1107/S09074449052925	RRID: SCR_014224	
software, algorithm	Axon pClamp 10.5	Axon (Molecular Devices)	RRID: SCR_011323	

368

369

370   *Cell line generation*

371   HEK293 (CRL-1573) cell lines were purchased from the American Type Culture Collection

372   (ATCC, Manassas, VA), and therefore were not further authenticated. The mycoplasma

373   contamination test was confirmed to be negative at ATCC.

374

375   *Purification of frPanx1-ΔLC*

376   frPanx1 (NP_001123728.1) was synthesized (Genscript) and cloned into the BamHI/ XhoI sites

377   of pCNG-FB7 vector containing a C-terminal Strep-tag II (WSHPQFEK). Amino acids from the

378   IL1 and IL2 were removed by standard PCR strategies, and the BamHI site was also removed

379   by quickchange mutagenesis. The full length frPanx1 and hPanx1 (NP_056183.2; synthesized

380   by Genscript) were also subcloned into pCNG-FB7 vectors by standard PCR. Sf9 cells were

381   infected with high titer baculovirus (20-25 mL P2 virus/ L cells) at a cell density of $2.5\text{-}3.0\times10^6$

382   cells/ mL and cultured at 27 °C for 48 hours. Cells were collected by centrifugation, washed

383   once with PBS, and lysed by nitrogen cavitation (4635 cell disruption vessel; Parr Instruments)

384   at 600 psi in PBS containing leupeptin (0.5 μg/mL), aprotinin (2 μg/mL), pepstatin A (0.5 μg/mL),

385   and phenylmethylsulfonyl fluoride (0.5 mM). Broken cells were centrifuged at 12,000 x g for 10

386 minutes, and membranes were collected by ultracentrifugation at 185,000 x g for 40 minutes.

387 Membranes were suspended and solubilized in PBS containing 1% C12E8 (Anatrace) for 40

388 minutes, followed by ultracentrifugation at 185,000 x g for 40 minutes. Solubilized material was

389 incubated with StrepTactin Sepharose High Performance resin (GE Healthcare) for 40 minutes

390 in batch. Resin was collected onto a gravity column (Bio-Rad), washed with 10 column volumes

391 of wash buffer (150 mM NaCl, 100 mM Tris-HCl pH 8.0, 1 mM EDTA, 0.5 mM C12E8), and

392 eluted with 5 column volumes of wash buffer supplemented with 2.5 mM desthiobiotin. Eluted

393 protein was concentrated and further purified on a Superose 6 10/300 Increase column (GE

394 Healthcare) with 150 mM NaCl, 10 mM Tris pH 8.0, 0.5 mM DDM as the running buffer. Peak

395 fractions were collected and pooled. All steps were performed at 4 °C or on ice.

396

397 *Reconstitution into nanodiscs*

398 MSP2N2 apolipoprotein was expressed and purified as described previously (Ritchie et al.,

399 2009), and the N-terminal His tag was cleaved off using TEV protease prior to use. To

400 incorporate frPanx1 into nanodiscs, soybean polar extract, MSP2N2 and frPanx were mixed at

401 final concentrations of 0.75, 0.3 and 0.3 mg/ml, respectively. The mixture was incubated end-

402 over-end for 1 hour at 4 °C, followed by detergent removal by SM2 Bio-Beads (Bio-Rad). The

403 supernatant and wash fractions were collected after an overnight incubation (~12 hours) and

404 further purified by size exclusion chromatography using a Superose 6 10/300 column in 20 mM

405 Tris-HCl pH 8.0, 150 mM NaCl, 1 mM EDTA. Peak fractions were pooled and concentrated to 3

406 mg/mL.

407

408 *Cryo-EM sample preparation and image collection*

409 frPanx1 in nanodiscs or hPanx1 in n-Dodecyl-β-D-Maltopyranoside (DDM; Anatrace) were

410 applied to glow-discharged lacey carbon coated copper grids (Electron Microscopy Services).

411 The grids were blotted for 4 s with blot force 7 at 85% humidity at 15 °C, and plunge frozen into

412   liquid ethane using a Vitrobot Mark IV (Thermo Fisher). All data were collected on a FEI Titan

413   Krios (Thermo Fisher) operated at an acceleration voltage of 300 keV. For frPanx1-ΔLC, a total

414   of 2034 images were collected at 130k magnification with a pixel size of 1.07 Å in electron

415   counting mode. Each micrograph was composed of 32 frames collected over 4 s at a dose of

416   1.79 e / Å^2 / frame and a total exposure per micrograph of 57.3 e / Å^2. Data were collected using

417   EPU software (FEI). For full-length frPanx1 in nanodiscs, a total of 574 images were collected at

418   130k magnification with a pixel size of 1.06 Å in electron counting mode. Each micrograph was

419   composed of 50 frames collected over 10 s at a dose of 1.4 e / Å^2 / frame. The total exposure

420   per micrograph was 70 e / Å^2. Data were collected using SerialEM (Schorb et al., 2019). Data

421   for full-length hPanx1 in DDM were collected in a similar fashion.

422

423   *Cryo-EM image processing and single particle analysis*

424   Warp was used for aligning movies, estimating the CTF and particle picking for frPanx1-ΔLC

425   and full-length hPanx1. For full-length frPanx1, movie alignment and CTF estimation were

426   performed using the program Unblur and CTFFind, respectively, within the cisTEM package

427   (Grant et al., 2018). 2D classification, ab-initio 3D map generation, 3D refinement, 3D

428   classification, per particle CTF refinement and B-factor sharpening were performed using the

429   program cisTEM (Grant et al., 2018). The single particle analysis workflow for frPanx1-ΔLC is

430   shown in Figure 1-figure supplement 3. De novo modeling was performed manually in Coot

431   (Emsley and Cowtan, 2004). The final model was refined against the cryo-EM map using

432   PHENIX real space refinement with secondary structure and Ramachandran restraints (Adams

433   et al., 2010). The FSCs were calculated by phenix.mtriage. Data collection and refinement

434   statistics are summarized in Extended data Table 1.

435

436   *Electrophysiology*

437 HEK293 cells were plated onto 12-mm glass coverslips (VWR) in wells of a 6-well plate and

438 transfected 24 hours later with 500-800 ng plasmid DNA using FUGENE 6 (Promega) according

439 to the manufacturer's instructions. Recordings were performed ~16-24 hours later using

440 borosilicate glass micropipettes (Harvard Apparatus) pulled and polished to a final resistance of

441 2-5 MΩ. Pipettes were backfilled with (in mM) 147 NaCl, 10 EGTA, 10 HEPES pH 7.0 with

442 NaOH. Patches were obtained in external buffer composed of (in mM) 147 NaCl, 10 HEPES pH

443 7.3 with NaOH, 13 glucose, 2 KCl, 2 CaCl$_2$, 1 MgCl$_2$. A rapid solution exchange system (RSC-

444 200; Bio-Logic) was used to perfuse cells with CBX or various salt solutions. Currents were

445 recorded using an Axopatch 200B amplifier (Axon Instruments), filtered at 2 kHz (Frequency

446 Devices), digitized with a Digidata 1440A (Axon Instruments) with a sampling frequency of 10

447 kHz, and analyzed with the pClamp 10.5 software (Axon Instruments). For voltage step

448 recordings, Panx1 expressing cells were held at -60 mV and stepped to various voltage

449 potentials for 1 s in 20 mV increments before returning to -60 mV. For ramp recordings, cells

450 were held at -60 mV, and ramped between -100 mV and + 100 mV over 3s duration.

451

452

461

462 **Author information**

463   **Kevin Michalski**

464   Present address: WM Keck Structural Biology Laboratory, Cold Spring Harbor Laboratory, Cold

465   Spring Harbor, NY, USA

466   **Julia Kumpf**

467   Present address: Brookline High School, 115 Greenough Street, Brookline, MA, USA

468

469   **References**

470   Adams, P.D., P.V. Afonine, G. Bunkoczi, V.B. Chen, I.W. Davis, N. Echols, J.J. Headd, L.W.
471   Hung, G.J. Kapral, R.W. Grosse-Kunstleve, A.J. McCoy, N.W. Moriarty, R. Oeffner, R.J.
472   Read, D.C. Richardson, J.S. Richardson, T.C. Terwilliger, and P.H. Zwart. 2010.
473   PHENIX: a comprehensive Python-based system for macromolecular structure solution.
474   *Acta Crystallogr D Biol Crystallogr*. 66:213-221.
475   Baker, N.A., D. Sept, S. Joseph, M.J. Holst, and J.A. McCammon. 2001. Electrostatics of
476   nanosystems: application to microtubules and the ribosome. *Proc Natl Acad Sci U S A*.
477   98:10037-10041.
478   Bao, L., S. Locovei, and G. Dahl. 2004. Pannexin membrane channels are mechanosensitive
479   conduits for ATP. *FEBS Lett*. 572:65-68.
480   Billaud, M., Y.H. Chiu, A.W. Lohman, T. Parpaite, J.T. Butcher, S.M. Mutchler, L.J. DeLalio, M.V.
481   Artamonov, J.K. Sandilos, A.K. Best, A.V. Somlyo, R.J. Thompson, T.H. Le, K.S.
482   Ravichandran, D.A. Bayliss, and B.E. Isakson. 2015. A molecular signature in the
483   pannexin1 intracellular loop confers channel activation by the alpha1 adrenoreceptor in
484   smooth muscle cells. *Sci Signal*. 8:ra17.
485   Billaud, M., A.W. Lohman, A.C. Straub, R. Looft-Wilson, S.R. Johnstone, C.A. Araj, A.K. Best,
486   F.B. Chekeni, K.S. Ravichandran, S. Penuela, D.W. Laird, and B.E. Isakson. 2011.
487   Pannexin1 regulates alpha1-adrenergic receptor- mediated vasoconstriction. *Circ Res*.
488   109:80-85.
489   Boassa, D., C. Ambrosi, F. Qiu, G. Dahl, G. Gaietta, and G. Sosinsky. 2007. Pannexin1
490   channels contain a glycosylation site that targets the hexamer to the plasma membrane.
491   *The Journal of biological chemistry*. 282:31733-31743.
492   Bravo, D., P. Ibarra, J. Retamal, T. Pelissier, C. Laurido, A. Hernandez, and L. Constandil. 2014.
493   Pannexin 1: a novel participant in neuropathic pain signaling in the rat spinal cord. *Pain*.
494   155:2108-2115.
495   Bruzzone, R., S.G. Hormuzdi, M.T. Barbe, A. Herb, and H. Monyer. 2003. Pannexins, a family
496   of gap junction proteins expressed in brain. *Proc Natl Acad Sci U S A*. 100:13644-13649.
497   Chekeni, F.B., M.R. Elliott, J.K. Sandilos, S.F. Walk, J.M. Kinchen, E.R. Lazarowski, A.J.
498   Armstrong, S. Penuela, D.W. Laird, G.S. Salvesen, B.E. Isakson, D.A. Bayliss, and K.S.
499   Ravichandran. 2010. Pannexin 1 channels mediate 'find-me' signal release and
500   membrane permeability during apoptosis. *Nature*. 467:863-867.
501   Chiu, Y.H., X. Jin, C.B. Medina, S.A. Leonhardt, V. Kiessling, B.C. Bennett, S. Shu, L.K. Tamm,
502   M. Yeager, K.S. Ravichandran, and D.A. Bayliss. 2017. A quantized mechanism for
503   activation of pannexin channels. *Nature communications*. 8:14324.
504   Chiu, Y.H., K.S. Ravichandran, and D.A. Bayliss. 2014. Intrinsic properties and regulation of
505   Pannexin 1 channel. *Channels (Austin)*. 8:103-109.
506   Chiu, Y.H., M.S. Schappe, B.N. Desai, and D.A. Bayliss. 2018. Revisiting multimodal activation
507   and channel properties of Pannexin 1. *J Gen Physiol*. 150:19-39.
508   Choi, W., N. Clemente, W. Sun, J. Du, and W. Lu. 2019. The structures and gating mechanism
509   of human calcium homeostasis modulator 2. *Nature*. 576:163-167.
510   Dahl, G. 2015. ATP release through pannexon channels. *Philos Trans R Soc Lond B Biol Sci*.
511   370.
512   Deneka, D., M. Sawicka, A.K.M. Lam, C. Paulino, and R. Dutzler. 2018. Structure of a volume-
513   regulated anion channel of the LRRC8 family. *Nature*. 558:254-259.
514   Emsley, P., and K. Cowtan. 2004. Coot: model-building tools for molecular graphics. *Acta
515   Crystallogr D Biol Crystallogr*. 60:2126-2132.
516   Giaume, C., L. Leybaert, C.C. Naus, and J.C. Saez. 2013. Connexin and pannexin
517   hemichannels in brain glial cells: properties, pharmacology, and roles. *Front Pharmacol*.
518   4:88.

519   Grant, T., A. Rohou, and N. Grigorieff. 2018. cisTEM, user-friendly software for single-particle
520   image processing. *eLife*. 7.
521   Kasuya, G., T. Nakane, T. Yokoyama, Y. Jia, M. Inoue, K. Watanabe, R. Nakamura, T.
522   Nishizawa, T. Kusakizako, A. Tsutsumi, H. Yanagisawa, N. Dohmae, M. Hattori, H. Ichijo,
523   Z. Yan, M. Kikkawa, M. Shirouzu, R. Ishitani, and O. Nureki. 2018. Cryo-EM structures
524   of the human volume-regulated anion channel LRRC8. *Nat Struct Mol Biol*. 25:797-804.
525   Kawate, T., and E. Gouaux. 2006. Fluorescence-detection size-exclusion chromatography for
526   precrystallization screening of integral membrane proteins. *Structure*. 14:673-681.
527   Kefauver, J.M., K. Saotome, A.E. Dubin, J. Pallesen, C.A. Cottrell, S.M. Cahalan, Z. Qiu, G.
528   Hong, C.S. Crowley, T. Whitwam, W.H. Lee, A.B. Ward, and A. Patapoutian. 2018.
529   Structure of the human volume regulated anion channel. *eLife*. 7.
530   Kronengold, J., M. Srinivas, and V.K. Verselis. 2012. The N-terminal half of the connexin protein
531   contains the core elements of the pore and voltage gates. *J Membr Biol*. 245:453-463.
532   Kucukelbir, A., F.J. Sigworth, and H.D. Tagare. 2014. Quantifying the local resolution of cryo-
533   EM density maps. *Nat Methods*. 11:63-65.
534   Kyle, J.W., P.J. Minogue, B.C. Thomas, D.A. Domowicz, V.M. Berthoud, D.A. Hanck, and E.C.
535   Beyer. 2008. An intact connexin N-terminus is required for function but not gap junction
536   formation. *J Cell Sci*. 121:2744-2750.
537   Locovei, S., J. Wang, and G. Dahl. 2006. Activation of pannexin 1 channels by ATP through
538   P2Y receptors and by cytoplasmic calcium. *FEBS Lett*. 580:239-244.
539   Lohman, A.W., I.L. Leskov, J.T. Butcher, S.R. Johnstone, T.A. Stokes, D. Begandt, L.J. DeLalio,
540   A.K. Best, S. Penuela, N. Leitinger, K.S. Ravichandran, K.Y. Stokes, and B.E. Isakson.
541   2015. Pannexin 1 channels regulate leukocyte emigration through the venous
542   endothelium during acute inflammation. *Nature communications*. 6:7965.
543   Ma, W., V. Compan, W. Zheng, E. Martin, R.A. North, A. Verkhratsky, and A. Surprenant. 2012.
544   Pannexin 1 forms an anion-selective channel. *Pflugers Arch*. 463:585-592.
545   Ma, Z., J.E. Tanis, A. Taruno, and J.K. Foskett. 2016. Calcium homeostasis modulator
546   (CALHM) ion channels. *Pflugers Arch*. 468:395-403.
547   Maeda, S., S. Nakagawa, M. Suga, E. Yamashita, A. Oshima, Y. Fujiyoshi, and T. Tsukihara.
548   2009. Structure of the connexin 26 gap junction channel at 3.5 A resolution. *Nature*.
549   458:597-602.
550   Michalski, K., E. Henze, P. Nguyen, P. Lynch, and T. Kawate. 2018. The weak voltage
551   dependence of pannexin 1 channels can be tuned by N-terminal modifications. *J Gen
552   Physiol*. 150:1758-1768.
553   Michalski, K., and T. Kawate. 2016. Carbenoxolone inhibits Pannexin1 channels through
554   interactions in the first extracellular loop. *J Gen Physiol*. 147:165-174.
555   Mousseau, M., N.E. Burma, K.Y. Lee, H. Leduc-Pessah, C.H.T. Kwok, A.R. Reid, M. O'Brien, B.
556   Sagalajev, J.A. Stratton, N. Patrick, P.L. Stemkowski, J. Biernaskie, G.W. Zamponi, P.
557   Salo, J.J. McDougall, S.A. Prescott, J.R. Matyas, and T. Trang. 2018. Microglial
558   pannexin-1 channel activation is a spinal determinant of joint pain. *Sci Adv*. 4:eaas9846.
559   Okada, Y., T. Okada, M.R. Islam, and R.Z. Sabirov. 2018. Molecular Identities and ATP
560   Release Activities of Two Types of Volume-Regulatory Anion Channels, VSOR and
561   Maxi-Cl. *Curr Top Membr*. 81:125-176.
562   Osei-Owusu, J., J. Yang, M.D.C. Vitery, and Z. Qiu. 2018. Molecular Biology and Physiology of
563   Volume-Regulated Anion Channel (VRAC). *Curr Top Membr*. 81:177-203.
564   Oshima, A., T. Matsuzawa, K. Murata, K. Tani, and Y. Fujiyoshi. 2016. Hexadecameric structure
565   of an invertebrate gap junction channel. *Journal of molecular biology*. 428:1227-1236.
566   Panchin, Y., I. Kelmanson, M. Matz, K. Lukyanov, N. Usman, and S. Lukyanov. 2000. A
567   ubiquitous family of putative gap junction molecules. *Curr Biol*. 10:R473-474.
568   Pelegrin, P., and A. Surprenant. 2006. Pannexin-1 mediates large pore formation and
569   interleukin-1beta release by the ATP-gated P2X7 receptor. *Embo J*. 25:5071-5082.

570 Ritchie, T.K., Y.V. Grinkova, T.H. Bayburt, I.G. Denisov, J.K. Zolnerciks, W.M. Atkins, and S.G.
571   Sligar. 2009. Chapter 11 - Reconstitution of membrane proteins in phospholipid bilayer
572   nanodiscs. *Methods in enzymology*. 464:211-231.
573 Romanov, R.A., M.F. Bystrova, O.A. Rogachevskaya, V.B. Sadovnikov, V.I. Shestopalov, and
574   S.S. Kolesnikov. 2012. The ATP permeability of pannexin 1 channels in a heterologous
575   system and in mammalian taste cells is dispensable. *J Cell Sci*. 125:5514-5523.
576 Sandilos, J.K., Y.H. Chiu, F.B. Chekeni, A.J. Armstrong, S.F. Walk, K.S. Ravichandran, and D.A.
577   Bayliss. 2012. Pannexin 1, an ATP release channel, is activated by caspase cleavage of
578   its pore-associated C-terminal autoinhibitory region. *J Biol Chem*. 287:11303-11311.
579 Schorb, M., I. Haberbosch, W.J.H. Hagen, Y. Schwab, and D.N. Mastronarde. 2019. Software
580   tools for automated transmission electron microscopy. *Nat Methods*. 16:471-477.
581 Schrodinger, LLC. 2015. The PyMOL Molecular Graphics System, Version 1.8. *In*.
582 Smart, O.S., J.G. Neduvelil, X. Wang, B.A. Wallace, and M.S. Sansom. 1996. HOLE: a program
583   for the analysis of the pore dimensions of ion channel structural models. *J Mol Graph*.
584   14:354-360, 376.
585 Syrjanen, J.L., K. Michalski, T.H. Chou, T. Grant, S. Rao, N. Simorowski, S.J. Tucker, N.
586   Grigorieff, and H. Furukawa. 2020. Structure and assembly of calcium homeostasis
587   modulator proteins. *Nat Struct Mol Biol*.
588 Thompson, R.J., M.F. Jackson, M.E. Olah, R.L. Rungta, D.J. Hines, M.A. Beazely, J.F.
589   MacDonald, and B.A. MacVicar. 2008. Activation of pannexin-1 hemichannels augments
590   aberrant bursting in the hippocampus. *Science*. 322:1555-1559.
591 Wang, J., C. Ambrosi, F. Qiu, D.G. Jackson, G. Sosinsky, and G. Dahl. 2014. The membrane
592   protein Pannexin1 forms two open-channel conformations depending on the mode of
593   activation. *Sci Signal*. 7:ra69.
594 Wang, J., and G. Dahl. 2010. SCAM analysis of Panx1 suggests a peculiar pore structure. *J*
595   *Gen Physiol*. 136:515-527.
596 Weaver, J.L., S. Arandjelovic, G. Brown, K.M. S, S.S. M, M.W. Buckley, Y.H. Chiu, S. Shu, J.K.
597   Kim, J. Chung, J. Krupa, V. Jevtovic-Todorovic, B.N. Desai, K.S. Ravichandran, and D.A.
598   Bayliss. 2017. Hematopoietic pannexin 1 function is critical for neuropathic pain. *Sci Rep*.
599   7:42550.

600

601